

# Feasibility of resolution-enhanced burst-mode interferometry in bistatic SAR

Virginie Kubica, Xavier Neyt

Electrical Engineering Dept., Royal Military Academy, Belgium

[Virginie.Kubica@elec.rma.ac.be](mailto:Virginie.Kubica@elec.rma.ac.be)

[Xavier.Neyt@elec.rma.ac.be](mailto:Xavier.Neyt@elec.rma.ac.be)

**Abstract**—Opportunistic SAR interferometry using a ground-based receiver and a spaceborne transmitter has previously been addressed. However, the analysis is limited to the conventional Stripmap mode of such radar satellites. The occurrence of satellite passes in Stripmap high-resolution mode is however not as frequent as passes in ScanSAR mode, hence the motivation to exploit ScanSAR mode illuminations by opportunistic receiver.

In ScanSAR mode imaging, a burst-mode resolution enhancement method has been developed to enhance the cross-range resolution performance by exploiting the sidelobe emissions of the beams illuminating the adjacent sub-swaths.

In this paper, the impact of this method on the interferometric performance is evaluated in the novel application of bistatic interferometry using cross-range resolution-enhanced burst-mode images.

## I. INTRODUCTION

Opportunistic Synthetic Aperture Radar (SAR) interferometry using a ground-based receiver and a spaceborne transmitter is a well-known topic. Applications such as Digital Elevation Model (DEM) generation [1]–[3] or Moving Target Indication (MTI) [4], [5] have been extensively studied. However, the analysis is limited to the conventional Stripmap mode of such radar satellites. The occurrence of satellite passes in Stripmap high-resolution mode is however not as frequent as passes in ScanSAR mode. The exploitation of this wide-swath synthetic aperture technique permits more frequent revisits of a given area.

For satellite passes exhibiting a favourable geometry, the burst-mode resolution enhancement method, described in [6], exploits the sidelobe radiations of the adjacent ScanSAR beams. This method can restore the cross-range resolution of the Stripmap mode, provided that the amplitude of the signals transmitted in the sidelobes is sufficient. However, this method has the drawback of increasing the noise content in the SAR image. Using this technique in bistatic interferometry will result in an increase in opportunities to obtain high resolution interferograms.

In this paper, the impact of the noise amplification on the interferometric performance is evaluated in the novel application of bistatic interferometry using cross-range resolution-enhanced burst-mode images.

The paper is organized as follows. The first section describes the designed passive bistatic radar and the bistatic geometry. In Section III, the burst-mode resolution enhancement method is reviewed and evaluated with real measurements. Section IV

analyzes the impact of the burst-mode resolution enhancement method in bistatic interferometry. Finally, the conclusion and our plan for further work are presented in Section V.

## II. PASSIVE SAR SYSTEM

The bistatic imaging radar consists of an opportunistic spaceborne transmitter and a ground-based receiver (Fig. 1). We use a backscattering geometry, where the receive and the transmit antennas are located on the same side of the observation area, to achieve the best possible range resolution [7]. This bistatic geometry offers the ability to receive echoed signals coming from the sidelobes' illumination of the transmit antenna. Note that the transmit signal in the sidelobes is only attenuated by the one-way transmit antenna gain pattern. Besides, the receiver is close to the observed area resulting in a smaller free space loss attenuation than in the monostatic case.

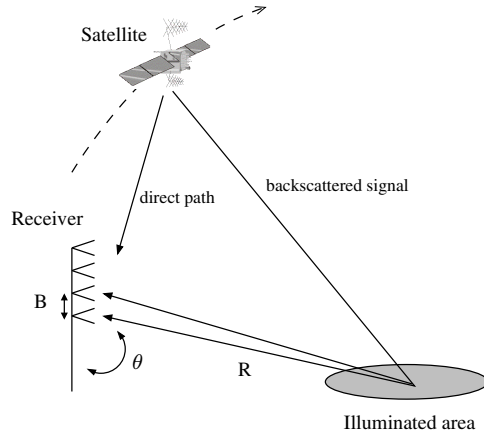


Fig. 1. Geometry for bistatic SAR.

The receiver, which is extensively described in [8], consists of a four-element antenna array followed by four heterodyne channels tailored for C-band. The receive antennas are separated vertically to allow across-track interferometry.

After a cascade of Low Noise Amplifiers, the four signals are down-converted to an intermediate frequency and then low-pass filtered. They are fed into the analog to digital converter which samples at a rate of 50 MSamples/s using a 16-bit A/D card (AlazarTech ATS660). They are finally digitally down-converted to base-band.

Next, signal separation is performed to extract the reference signal (direct-path signal) from the reflected signal. In the present case, the reference signal is re-synthesized since its general shape is known. Finally, an image is synthesized from the separated signals using a bistatic back-projection algorithm [9].

### III. BURST-MODE RESOLUTION ENHANCEMENT METHOD

Radar satellites such as ENVISAT, RADARSAT-2 or the future Sentinel-1, can operate in burst-mode: the antenna is steered in elevation to scan different sub-swaths. This allows to image larger swath (e.g. for global monitoring) at the expense of a degraded cross-range resolution [10].

In monostatic SAR, the burst nature of the ScanSAR signal leads to gaps in the azimuthal phase history which, if ignored, create grating lobes in the cross-range direction. Post-processing methods [11], [12] are thus essential to overcome this problem.

In opportunistic SAR for a receiver close to the imaged area, the bistatic geometry offers the opportunity, in some favourable geometries, to fill the aforementioned gaps by the sidelobe emissions of the adjacent beams. This allows to reduce the undesirable grating lobes without further degrading the cross-range resolution. To further improve the performance, the burst-mode resolution enhancement method [6] was developed to compensate this azimuthal amplitude modulation causing those azimuthal artifacts.

This section contains an in-depth analysis of this novel method using first simulated data and then, real measurements. The present analysis is based on ENVISAT measurements but may be extended to any other burst-mode SAR satellite.

#### A. Signal Model

The azimuth amplitude modulated signal can be modeled by

$$y(t) = w(t)x(t) + n(t) \quad (1)$$

where  $y(t)$  is the ScanSAR azimuth amplitude modulated signal with  $t$  the slow-time,  $x(t)$  the echoed signal (pulses) assuming a constant amplitude (independent of the ScanSAR beam),  $w(t)$  an amplitude modulation function representing the transmitter antenna gain at the elevation of the receiver/imaged area and which varies with each ScanSAR beam and  $n(t)$  the noise (thermal noise and eventual interference from scatterers located in the main beam i.e. at another range than the range of interest).  $x(t)$  and  $n(t)$  are further assumed to be uncorrelated.

The modulation function  $w(t)$  depends on the position of the receiver/imaged area in the global swath, and thus on its elevation angle, i.e. the angle scatterer-transmitter-nadir. Figures 2 show the amplitude modulation function for two different ScanSAR passes of ENVISAT (Wide Swath Mode) over Brussels. If the receiver is at the very edge of the swath, only one beam during the along-track illumination will be received (Fig. 2 (a)), leading to gaps in the along-track direction. However, if the receiver and its surrounding are in

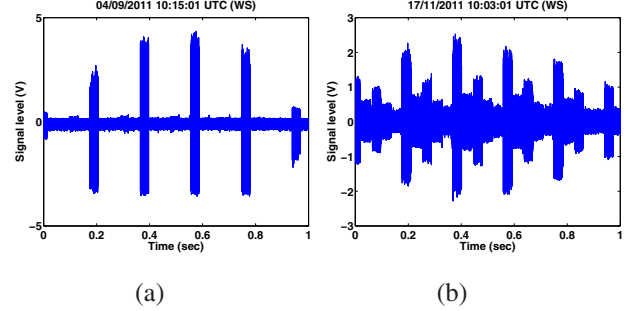


Fig. 2. Acquired ENVISAT's signals in Wide Swath mode: (a) single-beam illumination and (b) five-beam illumination.

the center of the swath (Fig. 2 (b)), the five beams are received and sidelobe imaging will be possible.

#### B. Optimum weighting function

The burst-mode resolution enhancement method consists in the estimation of  $x(t)$  given the measurement  $y(t)$ . The estimation of the unknown signal,  $x(t)$ , can be done by designing the function  $h(t)$  to minimize the Mean Square Error  $E[|x(t) - h(t)y(t)|^2]$  between the unknown true signal  $x(t)$  and its estimate  $h(t)y(t)$ , leading to the optimum weighting function

$$h_{opt}(t) = \frac{w(t)}{|w(t)|^2 + \frac{\sigma^2}{E[|x(t)|^2]}} = \frac{w(t)}{|w(t)|^2 + \frac{1}{\alpha}}, \quad (2)$$

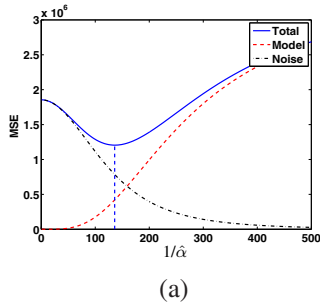
$\sigma^2$  being the variance of the noise.  $\alpha$  is the Signal to Noise Ratio (SNR) of the echoed signal after range compression.  $h(t)$  is optimum if  $\alpha$  is well-estimated. In practice, the SNR of the echoed signal  $x(t)$  is unknown and an estimated value,  $\hat{\alpha}$ , is considered.

To illustrate the importance of the correct estimation of  $\alpha$ , let us consider the Mean Square Error defined by

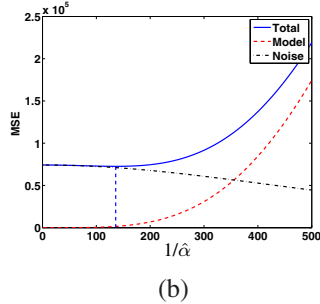
$$MSE = (w(t)h(t) - 1)^2 E[|x(t)|^2] + h(t)^2 \sigma^2, \quad (3)$$

with  $h(t)$  the weighting function corresponding to one estimated value of the SNR,  $\hat{\alpha}$ . The  $MSE$  reflects the tradeoff that  $h_{opt}(t)$  strives to achieve between the compensation of  $w(t)$  (first term), and thus the reduction of the grating lobes, and the amplification of the noise (second term). Figures 3 illustrate the two error contributions for two extreme values of  $w(t)$  for a range of  $\hat{\alpha}$ . The first term in (3) (red dashed curve), the model error, reflects the distance of  $h(t)$  from the inverse function  $\frac{1}{w(t)}$ . The second term (black dash-dotted curve), the noise error, illustrates the amplification of the noise due to the application of the weighting function.

At the optimum (vertical line), the two error contributions are different depending on the amplitude of  $w(t)$  at a given slow-time. For a poor signal amplitude (Fig. 3 (a)),  $h_{opt}(t)$  will limit the noise amplification by differing from the inverse function. For a large signal amplitude (Fig. 3 (b)),  $h_{opt}(t)$  tends to the inverse function (reducing the model error) and, at the same time, will amplify the noise which has little consequences as the latter is, in this case, minor.



(a)



(b)

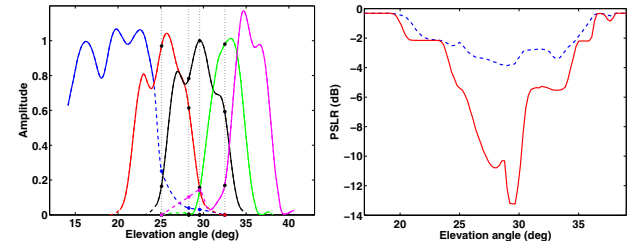
Fig. 3. Calculated Mean Square Error for different  $\hat{\alpha}$  for (a) a small value and (b) a large value of  $w(t)$ .

For an optimistic value of  $\hat{\alpha}$ , the signal as well as the noise will be compensated resulting in a reduction of the grating lobes due to the signal component and an increased noise level due to the amplification of the noise. For a pessimistic value of  $\hat{\alpha}$ , neither the noise component nor the signal component will be amplified leading to grating lobes of relatively high amplitude.

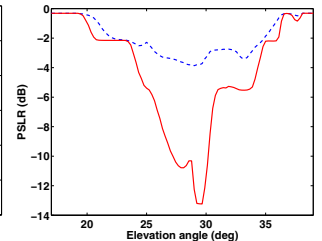
### C. Evaluation on real measurements

Each acquisition geometry is characterized by an azimuth amplitude modulation window,  $w(t)$ , which depends on the elevation angle at which the receiver/scatterers are located. Therefore, this key parameter can predict whether or not the planned ScanSAR pass is suitable for the use of the burst-mode resolution enhancement method. For performance prediction, knowledge of the amplitude of the sidelobes of the elevation diagram is of utmost importance. We did the evaluation exercise for the ASAR instrument on-board the ENVISAT spacecraft from the European Space Agency (ESA). As ESA only provides the antenna elevation diagram of the 5 beams of the ASAR antenna for  $5^\circ$  around the beam center, a six-month measurement campaign was performed to extrapolate the antenna elevation diagrams at other angles. On Fig. 4 (a), the coloured dots on the dashed line denote our measurements and the black dots on the solid line denote the values obtained from sampling the antenna patterns provided by ESA.

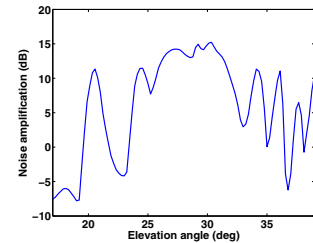
To illustrate the azimuth amplitude compensation method, a point scatterer with a SNR of  $-10$  dB (before coherent processing) with different satellite passes over  $15^\circ \leq \theta_{el} \leq 40^\circ$  is simulated. Then, the Peak-to-SideLobe Ratio<sup>1</sup> (PSLR) of the Impulse Response Function (IRF) along a one-dimensional profile (in the cross-range direction here) is computed to assess the reduction of the grating lobes on the IRF. Figure 4 (b) shows the PSLRs of the IRF obtained with the conventional matched-filter with and without azimuth amplitude compensation. This latter was performed using the optimum weighting function,  $h_{opt}$ . For  $27^\circ \leq \theta_{el} \leq 32^\circ$ , the PSLR of the matched-filter output with the compensation method is by far better than without. Outside that angular range, one or several beams are barely present leading to a poor signal amplitude over part of  $w(t)$ . In those cases,  $h_{opt}$  will neither amplify the signal



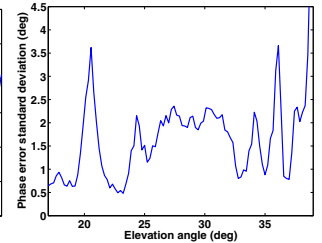
(a)



(b)



(c)



(d)

Fig. 4. (a) Extrapolated antenna elevation diagram of ESA, (b) calculated PSLR for different antenna elevation angles without compensation (dashed line) and with compensation (solid line), (c) calculated relative noise energy (w.r.t. Stripmap mode) amplification of the compensation method and (d) estimated standard deviation of the phase noise error due to the application of the compensation method.

nor the noise: the poor SNR will not degrade but the grating lobes will remain. Figure 4 (c) depicts the corresponding noise amplification effect due to the application of the optimum weighting function. The reduction of the grating lobes is accompanied by a noise amplification by up to 15 dB. Note that the optimum weighting function minimizes the Mean Square Error and not the PSLR. Minimizing the PSLR would lead to a higher amplification of the noise.

## IV. BISTATIC SCANSAR INTERFEROMETRY

In this section, the impact of the proposed cross-range resolution enhancement method in interferometry is illustrated using first simulated data and then, real measurements. One processing artifact of the proposed method is the increase of the noise content in SAR images. In interferometry, this can lead to a partial decorrelation of the two images which introduces noise in the interferogram and corrupts the estimation of the interferometric phase.

### A. Performance evaluation on simulated data

Single-pass interferometry is considered throughout this analysis to concentrate on the study of the phase noise generated by the cross-range resolution enhancement method. Indeed, the phase noise due to temporal change of the scene vanishes. The single-pass interferometric images are assumed to be obtained using two receiving antennas separated by a vertical baseline and the satellite ENVISAT as transmitter of opportunity.

<sup>1</sup>The PSLR is defined as the ratio of the peak intensity of the most intense sidelobe to the peak intensity in the mainlobe.

1) *Impact on the interferometric phase*: We evaluate the phase noise added by the cross-range resolution enhancement method at a given pixel through a Monte Carlo simulation (100 realizations). A scenario similar to that of Section III-C (SNR of  $-10$  dB) is considered. The standard deviation of the phase error on the simulated point scatterer is evaluated for, first, Stripmap passes, taken as reference, and then ScanSAR passes with the burst-mode resolution enhancement method. Figure 4 (d) shows the standard deviation of the phase error in the compensated ScanSAR mode as a function of the elevation angle. As expected, both curves (Fig. 4 (c) and (d)) tend to follow a similar pattern: for large noise amplification factors, the standard deviation of the phase error is significant. The phase noise for the Stripmap mode has a standard deviation of  $0.27^\circ$  which is negligible. However, in ScanSAR mode, the cross-range resolution enhancement method adds a phase noise component which can reach a standard deviation of  $3.5^\circ$ . The choice of the vertical baseline will determine the impact of the phase noise on the height.

For a specific favourable geometry ( $\theta_{el} = 29^\circ$ ), the phase noise contribution of the cross-range resolution enhancement method can be evaluated considering different SNRs. For this acquisition geometry, the noise amplification due to the cross-range resolution enhancement method reaches  $10$  dB (Fig. 4 (c)). Table I gives the sample standard deviation of the

TABLE I  
SAMPLE STANDARD DEVIATION OF THE PHASE ERROR FOR  $\theta_{el} = 29^\circ$

SNR (dB)	Stripmap		Compensated ScanSAR	
	$\sigma(\delta\phi)$ ( $^\circ$ )	$\delta H$ (m)	$\sigma(\delta\phi)$ ( $^\circ$ )	$\delta H$ (m)
-10	0.27	0.07	2.13	0.59
-20	0.81	0.22	3.09	0.85
-30	2.73	0.75	6.90	1.91

phase error,  $\sigma(\delta\phi)$ , for different SNRs. Those sample standard deviations are estimated based on 100 realizations. Assuming the distribution of the phase error to be Gaussian, the error made on those estimates is of the order of 7% of the estimated value.

As can be expected, for lower SNRs, the phase standard deviation degrades in both modes.

Let us consider the geometry of Fig. 1 to relate this phase error to a height error information. The relationship between the interferometric phase error,  $\delta\phi$ , and the height error,  $\delta H$  is as follows

$$\delta H = \frac{\lambda}{2\pi} \frac{R}{B} \delta\phi, \quad (4)$$

with  $\lambda$  the wavelength,  $B$  the vertical baseline and  $R$  the distance from the scene to the receiver. This last formula is valid if the scene is seen from the same incident angle,  $\theta$ , from both receiving antennas, i.e. for small baselines. The height error of Table I is computed for a small baseline equals to  $5\lambda$  and for a scene at a distance of 500 m from the receiver. The Stripmap processing can handle very low SNR while the compensated ScanSAR processing shows its limitations from SNR of  $-30$  dB with a height error of 2 m.

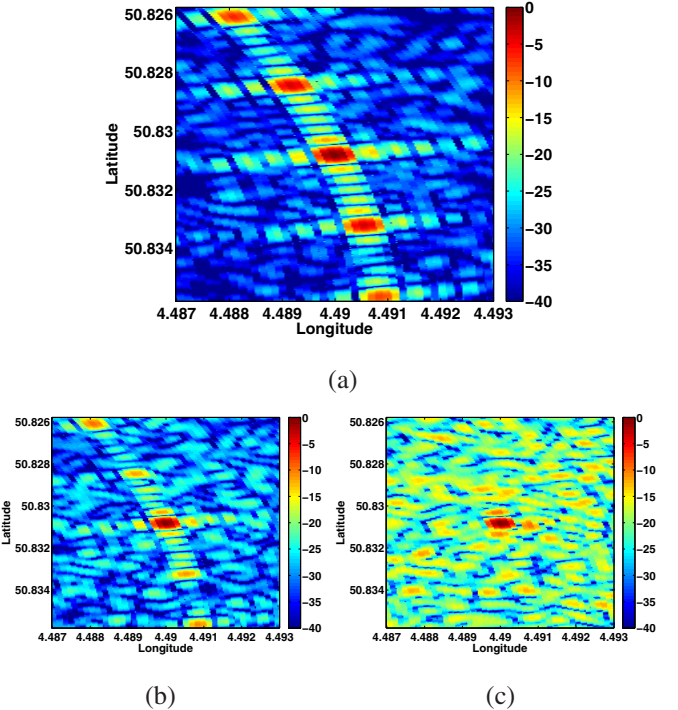


Fig. 5. SNR =  $-10$  dB: (a) Zoom on a simulated point scatterer in the SAR image, (b) the azimuth amplitude compensated SAR image with the optimum weighting function and (c) with a sub-optimal weighting function (inverse filter).

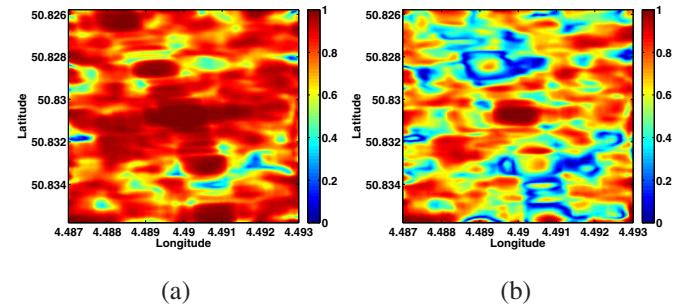


Fig. 6. Coherence images between the non-compensated and the compensated SAR image (simulated data) (a) with the optimum weighting function and (b) with a sub-optimal weighting function (inverse filter).

2) *Impact on the coherence*: The impact of the amplification of the noise of the cross-range resolution enhancement method can also be assessed by computing the coherence image between the SAR image and the amplitude compensated SAR image. The coherence parameter refers to the amplitude of the complex correlation coefficient between two SAR images. Given the SAR images  $z_1$  and  $z_2$ , the complex correlation coefficient is defined as [13]

$$\Delta = \frac{E[z_1 z_2^*]}{\sqrt{E[|z_1|^2]} \sqrt{E[|z_2|^2]}} \quad (5)$$

where  $*$  refers to the complex conjugation and  $E[.]$  is the expectation operator. In practice,  $\Delta$  can be estimated from (5) by substituting the ensemble averages with spatial sampled averages (i.e. by assuming process ergodicity in a small

estimation area of  $L \times L$  pixels). Thus, the sample coherence  $\delta$  is

$$\delta = \frac{\sum_{i=1}^L z_{1i} z_{2i}^*}{\sqrt{\sum_{i=1}^L |z_{1i}|^2} \sqrt{\sum_{i=1}^L |z_{2i}|^2}} \quad (6)$$

with  $L$  the number of pixels used to estimate the coherence. A high coherence level (close to 1) indicates a very good phase correlation between the two images.

Figure 5 (a) shows the simulated Single-Look Complex (SLC) SAR image centered on the point scatterer with a SNR of  $-10$  dB (before coherent processing). The expected grating lobes in azimuth along the isorange can be observed. If the cross-range resolution enhancement method is applied with the optimum value of  $\hat{\alpha}$ , there is a tradeoff between the amplification of the noise and the reduction of the grating lobes. The latter are reduced but still present on Fig. 5 (b). Figure 6 (a) depicts the coherence image between the SAR images illustrated on Fig. 5 (a) and (b). The observed high coherence reflects a small amplification of the noise by the cross-range resolution enhancement method. For a high value of  $\hat{\alpha}$ , the weighting function  $h(t)$  becomes the inverse of  $w(t)$ : the amplitude modulation of the signal  $x(t)$  is compensated at the expense of an increase of the noise content in the SAR image (Fig. 5 (c)). This amplification of the noise leads to a coherence loss between the SAR images illustrated on Fig. 5 (a) and (c) as shown on the coherence image (Fig. 6 (b)).

### B. Performance evaluation on experimental data

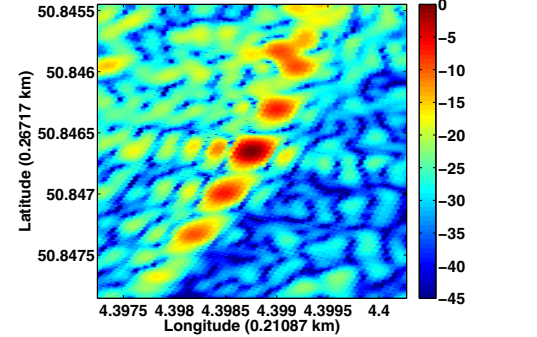
On the 30<sup>th</sup> of April 2013, the receiver, located in Brussels, was in the centre of the swath of the Canadian satellite RADARSAT-2 operating in the ScanSAR Wide mode (SWB). To illustrate the performance of the cross-range resolution enhancement method, a point-like target in the image is analyzed. Figure 7 (a) shows one of the four SLC georeferenced SAR image centered on the point scatterer. A processing similar to that of Section IV-A2 is performed and is illustrated on Fig. 7 (b) and (c). The results on the coherence images of Fig. 8 lead to the same conclusion as with simulated data.

## V. CONCLUSION

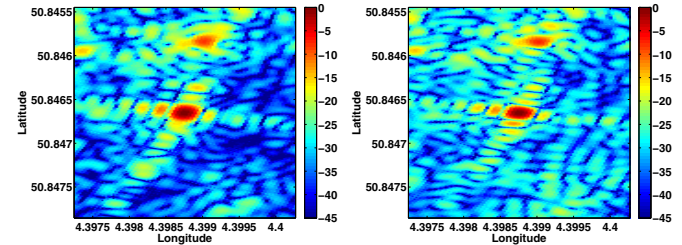
In this paper, we have shown how, in favourable geometries, the burst-mode resolution enhancement method can recover the cross-range resolution of the Stripmap mode at the expense of the amplification of the existing noise. The impact of the increase of the noise content in SAR images has been simulated and studied leading to the conclusion that the phase error induced by the burst-mode resolution enhancement method has only a minor effect on the accuracy of height estimation at typical SNRs.

The preliminary results on real measurement have highlighted the benefits of the burst-mode resolution enhancement method. Indeed, for the optimum implementation of the method, the decorrelation caused by the noise amplification is very limited while the grating lobes are significantly reduced.

In further research, the practical effectiveness of the burst-mode resolution enhancement method will be demonstrated in the interferometric processing chain for DEM reconstruction.



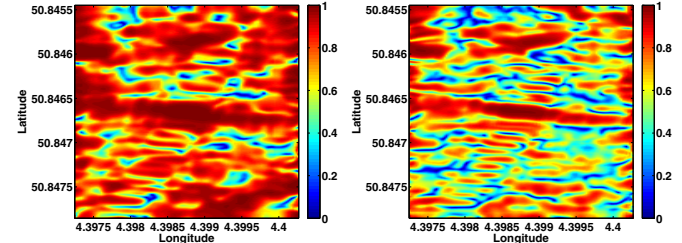
(a)



(b)

(c)

Fig. 7. (a) Zoom on a point scatterer in the georeferenced SAR image, (b) the azimuth amplitude compensated SAR image with the optimum weighting function and (c) with a sub-optimal weighting function (inverse filter).



(a)

(b)

Fig. 8. Coherence images between the non-compensated and the compensated SAR image (a) with the optimum weighting function and (b) with a sub-optimal weighting function (inverse filter).

## REFERENCES

- [1] S. Duque, P. Lopez-Dekker, J. J. Mallorqui, and J. C. Merlano, "Back and Forward Bistatic Interferometry," in *IEEE International Geoscience and Remote Sensing Symposium*, pp. III-601 – III-604, 2008.
- [2] S. Duque, P. Lopez-Dekker, and J. J. Mallorqui, "Single-Pass Bistatic SAR Interferometry Using Fixed-Receiver Configurations: Theory and Experimental Validation," *IEEE Transactions on Geoscience and Remote Sensing*, vol. 48, pp. 2740–2749, June 2010.
- [3] H. Nies, F. Behner, S. Reuter, O. Loffeld, and R. Wang, "Polarimetric and interferometric applications in a bistatic hybrid SAR mode using Terrasar-X," in *IEEE International Geoscience and Remote Sensing Symposium*, pp. 110–113, July 2010.
- [4] S. Duque, P. Lopez-Dekker, J. C. Merlano, and J. J. Mallorqui, "Bistatic SAR along track interferometry with multiple fixed receivers," in *IEEE International Geoscience and Remote Sensing Symposium*, pp. 4099–4102, July 2010.
- [5] P. Lopez-Dekker, S. Duque, J. C. Merlano, J. C. Rodriguez-Silva, and J. J. Mallorqui, "Fixed-Receiver Bistatic SAR Along-Track Interferom-

- etry: First Results," in *8th European Conference on Synthetic Aperture Radar*, pp. 1–4, June 2010.
- [6] V. Kubica and X. Neyt, "ScanSAR resolution enhancement in bistatic operation," in *IET International Conference on Radar Systems*, (Glasgow, UK), Oct. 2012.
  - [7] M. Cherniakov, "Space-surface bistatic synthetic aperture radar - prospective and problems," in *RADAR 02*, pp. 22–25, IEE, Oct. 2002.
  - [8] E. Cristofani, V. Kubica, and X. Neyt, "A multibeam opportunistic SAR system," in *IEEE Radar Conference*, (Kansas City, MI), May 2011.
  - [9] Y. Ding and D. Munson, "A fast back-projection algorithm for bistatic SAR imaging," in *Image Processing*, vol. 2, pp. 449–452, 2002.
  - [10] R. Raney, A. Luscombe, E. Langham, and S. Ahmed, "RADARSAT," *Proceedings of the IEEE*, vol. 79, pp. 839–849, June 1991.
  - [11] R. Bamler and M. Eineder, "ScanSAR Processing Using Standard High Precision SAR Algorithms," *IEEE Transactions on Geoscience and Remote Sensing*, vol. 34, pp. 212–218, Jan. 1996.
  - [12] J. Holzner and R. Bamler, "Burst-mode and ScanSAR interferometry," *IEEE Transactions on Geoscience and Remote Sensing*, vol. 40, no. 9, pp. 1917–1934, 2002.
  - [13] R. Touzi, A. Lopes, J. Bruniquel, and P. Vachon, "Coherence estimation for SAR imagery," *IEEE Trans. on Geoscience and Remote Sensing*, vol. 37, no. 1, pp. 135–149, 1999.